Reactor Design for Advanced Oxidation Processes

José L. Nava and Carlos Ponce de León

Abstract Electrochemical reactor design for oxidation processes follows similar engineering principles used for typical electrosynthesis reactors and include considerations of the components materials, electrode and cell geometries, mass transport conditions, rate of reactions, space–time yield calculations, selectivity, modeling, and energy efficiencies. It is common practice to optimize these characteristics at laboratory scale level followed by more practical considerations to build a larger reactor able to accomplish a required performance that can be easily assembled and requires low maintenance and monitoring. The scaling-up process should involve testing a variety of electrode configurations and cell designs to maximize the degradation of a particular pollutant. In this chapter, we describe the general principles of reactor design and list the most typical reactor configurations and performance followed by some recent advances in modeling and further developments.

Keywords Computational fluid dynamics, Current distributions, Electrochemical reactor, Filter-press flow cell, Mass transport, Non-ideal electrolyte flow, Packed bed electrode, Parallel plate electrodes, Rotating cylinder electrode, Wastewater treatment

J.L. Nava (✉)
Departamento de Ingeniería Geomática e Hidráulica, Universidad de Guanajuato, Av. Juárez 77, Guanajuato 3600, Mexico
e-mail: jlnm@ugto.mx

C. Ponce de León
Electrochemical Engineering Laboratory, Energy Technology Research Group, Faculty of Engineering and the Environment, University of Southampton, Highfield, Southampton SO17 1BJ, UK
e-mail: capla@soton.ac.uk

M. Zhou et al. (eds.), *Electro-Fenton Process: New Trends and Scale-Up*,
Hdb Env Chem (2018) 61: 263–286, DOI 10.1007/698_2017_54,

Contents

1 Introduction

Electrochemical engineering uses the principles of chemical engineering and electrochemical sciences in order to develop an interdisciplinary field that nowadays is very diversified and extensive, covering aspects of design and performance of electrochemical processes that might involve non-electrochemical aspects. Well-known electrochemical engineering processes include the chlor-alkali industry, inorganic synthesis, electrowinning, refining and recovering metals, redox flow batteries for energy storage, batteries, and fuel cells, and in recent years, the field has established new and effective methodologies for environmental remediation and pollution control. Electrochemical technologies have been typically used for metal recovery; however, advances also include electrochemical oxidation process for recalcitrant organic materials and the electrocoagulation process that has also been used for organic removal. This has been forced by government regulations to clean households and industrial wastewaters before disposal and the urgent need to include green and sustainable processes into the existing industrial manufacturing. This chapter considers the advances of cell design and architecture and electrode materials and analyzes current trends and developments.

Electrochemical advanced oxidation processes (EAOPs) are well-established technologies characterized by the production of highly active hydroxyl radicals ($^{\bullet}OH$) that can be divided into heterogeneous and homogenous processes. Typically, boron-doped diamond electrodes or photocatalytic surfaces such as TiO_2 generate the radical in the heterogeneous process, while in the homogeneous process, the radical is formed by the Fenton's Reaction by electrogenerated hydrogen peroxide and Fe^{2+} ions in solution. The electrochemical cell is the center of the EAOPs and requires careful consideration of suitable designs, electrodes, and whether or not a separator material between anode and cathode is necessary [1–3]. In most cases, the cell design should provide uniform current and potential distribution that promotes the optimization of parameters such as energy consumption and increases the oxidation rate and the selectivity.

2 Design and Basic Considerations

Typical electrochemical cell design includes the parallel plate electrode geometry which offers uniform current and potential distributions and is by far the most popular cell design used. This particular design allows easy control of the distance between the electrodes and high rates of mass transport when used in a flow cell. In addition, parallel plate electrodes cells can be scaled-up relatively easily into modules of up to 200 bipolar parallel plates. However, it is common to find the use of parallel plates or rod electrodes immersed in rounded beakers at laboratory scale reactors with nonuniform stirring patterns that generally provide poor current and potential distribution and the flow regime cannot be easily determined. In these works, mass transport effects cannot be quantified and are not conducive to scale up the systems. A typical example of a parallel plate reactor is shown in Fig. 1a, and some examples for the degradation of organic materials include the treatment of municipal solid waste leachate [4] and removal of pharmaceutical clofibric acid and dyes [5, 6] and reactive yellow [7]. Other reactor designs are also popular due to their versatility although they are not so easy to scale up as the parallel plate geometry includes rotating cylindrical electrodes (RCE). A typical configuration is presented in Fig. 1b, and some examples include the reduction of ferric ions for the removal of benzene sulfonic acid [8]. Another type of reactor less frequently used is the bipolar trickle tower containing three-dimensional electrodes layers (see Fig. 1c [9, 10]), the fluidized bed (see Fig. 1d [11–13]), and the H-type cells for the degradation of herbicide diquat dibromide [14] (see Fig. 1e) and rotating anodes to evaluate the perchlorate formation in drinking water disinfected by direct electrolysis [15]. In all these configurations, it is desirable that the reactors have the following characteristics [2]:

- Low cost of materials for construction, maintenance, and operation together with easy installation and simplicity during the scaling-up
- Low cell potential difference
- Low-pressure drop including manifolds and electrolyte compartment
- An undivided cell is preferred for simplicity and to keep costs low
- Large surface area electrodes working at uniform current density and potential
- High conversion rates that could be achieved with high rates of mass transport

The factors above are closely associated with the selection of electrode materials, membranes, flow regime, and type of operation. The following section outlines some of the materials used for advanced oxidation processes.

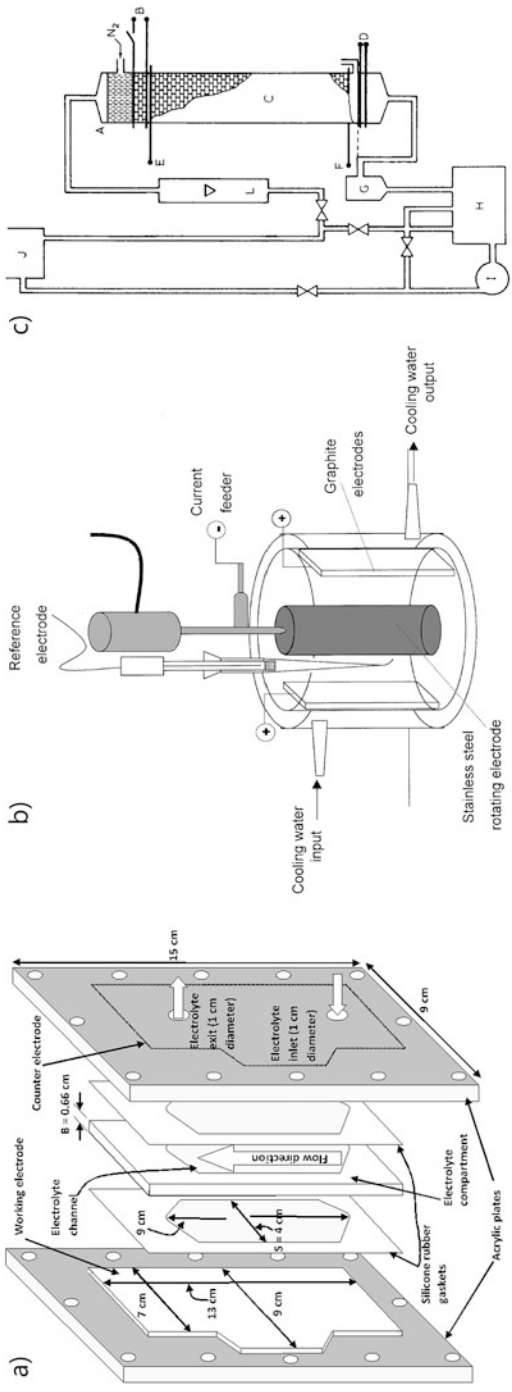

Fig. 1 Reactor configurations. (**a**) Parallel plate reprinted from [16], Copyright 2011, with permission from Elsevier, (**b**) rotating cylinder reprinted from [17], Copyright 2001, with permission from Elsevier, (**c**) bipolar trickle tower reprinted from [18], Copyright 1980, with permission from Springer, (**d**) fluidized bed reprinted from [11], Copyright 2010, with permission from Elsevier, and (**e**) H-type, reprinted from [14], Copyright 2017, with permission from Springer

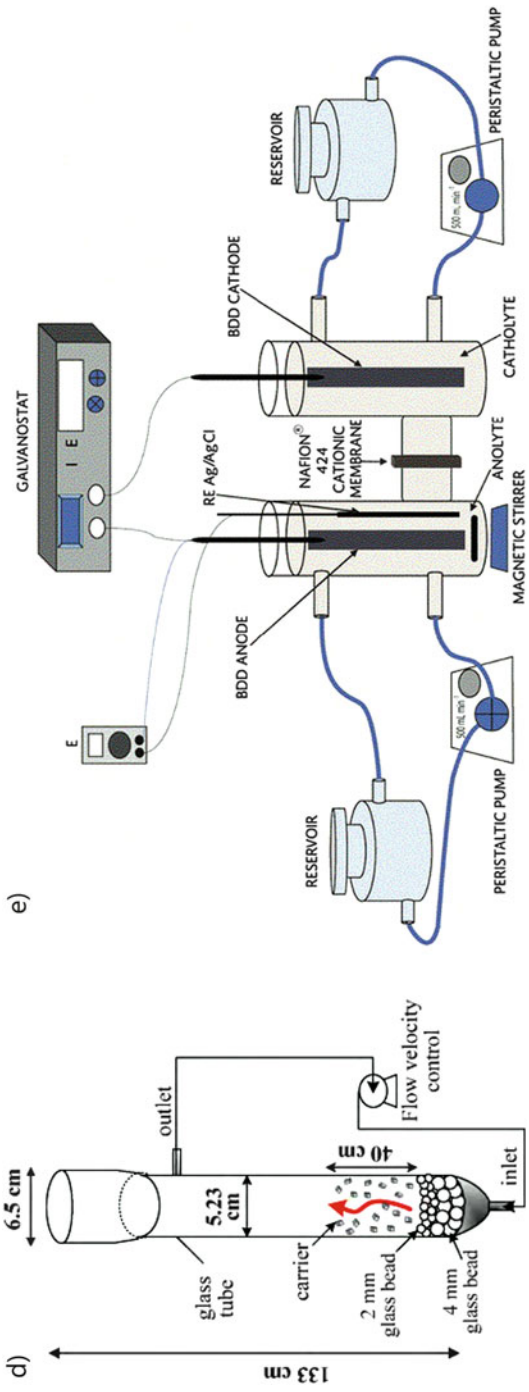

Fig. 1 (continued)

2.1 Electrode Materials

The selectivity and efficiency of the oxidation process is strongly dependent on the electrode material. Two types of anode materials have been generally accepted, which include electrodes with low overpotential for the oxygen evolution Reaction (OER) (active) and those with high overpotential for the OER (non-active) [19]. The active electrodes include most carbons and platinum, iridium, and ruthenium oxides based electrodes whereas those with high overpotential for OER are mainly antimony doped tin oxide, lead dioxide, and boron-doped diamond (BBD) electrodes. Carbon electrodes are used as cathodes for the generation of hydrogen peroxide to form the Fenton reagent for an indirect electrochemical oxidation. Many forms of carbon have been used and these include 3D electrodes such as reticulated vitreous carbon, felts, cloths, or gas diffusion electrodes (GDE) [20]. The manufacture of the GDE should pay attention to the hydrophobicity in order to avoid flooding the electrode while providing a 3-phase point of contact for electrolyte, gas, and catalyst. These electrodes overcome the problem of low solubility of oxygen in aqueous electrolytes by continuously supplying oxygen for the production of hydrogen peroxide and thus generate the Fenton reagent [21]. The most important characteristic of the electrode is the electroactive area. In a flat planar electrode fitted into a flow cell, the geometrical area is generally taken as the active electrode area whereas it is more difficult to determine the electroactive area for three-dimensional electrodes obtained from depositing nanostructured materials on a flat plate [22] or from using reticulated, meshed, or felt materials. The electroactive area should be as high as possible but avoiding high-pressure drops of the electrolyte flow or poor potential distribution generally encountered in 3D electrodes. Since the sections of the 3D electrodes are located at dissimilar distances from the counter electrode causing different surface potential and current densities, thin electrodes are preferred to minimize uneven distribution. The use of 3D BDD electrodes demonstrates the advantages of three-dimensional structures. For example, [23] recently demonstrated that using a 3D BBD electrode, organic pollutants such as phenols, aspirin, paracetamol, xylenol, and methyl orange and alizarin red S can be mineralized completely at higher rates compared to flat BDD electrodes, using the same electrical charge. A typical problem in three-dimensional electrodes is to achieve a good electrical contact with the current collector. Conductive glue or pressure is used, but the point of contact is always prone to corrosion and increases the overpotential.

The current intensity (I) on the electrode depends on the concentration gradient of the electroactive species between the bulk (c_b) and the surface (c_0) and the mass transport coefficient k_m:

$$I = n\,F\,A\,k_m(c_b - c_0\,) \tag{1}$$

where n, F, and A are the number of electrons exchanged, the Faraday constant, and the electroactive surface, respectively. At the mass transport limiting conditions, i.e., when $c_0 = 0$, the equation can be simplified to:

$$I_L = n\,F\,A\,k_m\,c_b \tag{2}$$

where I_L is the limiting current. In porous 3D electrodes operating under complete mass transport control such as reticulated materials, stack meshes, and packed beds, the area of the electrode can be considered as the area per unit volume A_e ($=A/V_e$) where V_e is the electrode volume. High values for the k_m and A_e are desirable to improve the reactor performance.

2.2 Cell Potential

In electrochemical rectors used for EAOPs, the ideal thermodynamic energy input is related to the Gibbs free energy change for the cell Reaction, ΔG_{cell}, which relates to the cell potential, E_{cell}, at the equilibrium:

$$\Delta G_{cell} = -nFE_{\ cell} \tag{3}$$

When the current or potential is applied at the limiting current conditions, the potential difference for any electrochemical cell is a complicated quantity with several contributions that depend on the electrolyte, electrode materials, and the equilibrium potentials of the anodic and cathodic reactions:

$$E_{cell} = E_c^0 - E_a^0 - \sum |\eta\,| - \sum |\mathrm{IR}| \tag{4}$$

The first and second terms on the right-hand side of Eq. (4) are the cathodic and anodic standard potentials, whereas the third and fourth terms correspond to the overpotentials and the electrical resistance of the components. These last two terms represent the inefficiencies of the system and lead to a higher cell voltage requiring additional energy to drive the Reaction. While there is some freedom to select the anodic and cathodic reactions, it is more common to minimize the last two terms. The overpotentials depend on the activation and mass transport polarization, which can be minimized by operating the reactor at high temperatures and by selecting an appropriate catalyst for the desired Reaction together with high rates of mass transport. The term can be expanded as:

$$\sum |\eta| = |\eta_{\text{c,act}}| + |\eta_{\text{a,act}}| + |\eta_{\text{c,conc}}| + |\eta_{\text{a,conc}}| \quad (5)$$

where $\eta_{\text{c, act}}$ and $\eta_{\text{a, act}}$ represent the electron transfer limitations and dominate at low currents, whereas the terms $\eta_{\text{c, conc}}$ and $\eta_{\text{a, conc}}$ are the mass transport limitations due to lack of supply of electroactive species and it is generally observed at high currents when the current being withdrawn is larger than the rate at which the electroactive species reach the electrode surface. The IR term can be expanded to:

$$\sum |\text{IR}| = |\text{IR}_{\text{c,circuit}}| + |\text{IR}_{\text{a,circuit}}| + |\text{IR}_{\text{catholyte}}| + |\text{IR}_{\text{anolyte}}| + |\text{IR}_{\text{membrane}}| \quad (6)$$

The equation clearly shows the need to minimize the resistance of the components of the electrochemical reactor, including electrolytes, electrodes, electrical components, current collectors, and the membrane in the case of divided cells.

2.3 Performance

One of the most relevant parameters to evaluate the reactor performance which is rarely reported in AOP is the space–time yield, ρ_{ST}, which represents the amount of material w, reacted per unit reactor volume V per unit time:

$$\rho_{\text{ST}} = \frac{1}{V}\frac{dw}{dt} = \frac{\varnothing I}{nFV} \quad (7)$$

where w is the mass of materials (kg), and ϕ is the current efficiency. Typical values of this parameter for electrochemical processes are in the order of 0.08–0.1 kg h^{-1} dm^{-3}, whereas for non-electrochemical processes the values range between 0.1 and 1 kg h^{-1} dm^{-3}. The challenge for electrochemical engineers is to increase this value and recent academic studies have tried to develop changes in cell design and electrodes.

In electrochemical process under kinetic control, the rate of electron transfer prevails and the Reaction rate depends on the electrode potential and the choice of catalyst; the electrode area should be high. Under these conditions, the current varies exponentially with the overpotential [24]:

$$I = nFAkc\exp\left(\frac{\alpha_a nF\eta}{RT}\right) \quad (8)$$

High surface area and active electrocatalyst promote high rate constants, k, which is related to the exchange current density j_0; α_{a} is the anodic charge transfer coefficient. Under these conditions, the secondary reactions are minimized. On the contrary, under full mass transport conditions the electroactive species are consumed immediately when they reach the electrode surface and the rate of reactant

supply or product removal dominates, the system operates at the maximum limiting current I_L. At these conditions, the convective-diffusion regime and the relative mean linear velocity u, of the electrolyte in a flow channel or the peripheral velocity of a rotating cylinder, to the electrode surface control the limiting current, where Eq. (2) is transformed into Eq. (9) [25]:

$$I_L = K\, u^{\omega} \tag{9}$$

where K is a constant given by the properties of the electrolyte composition and temperature while ω depends on geometry. Laminar flows are observed at $\omega = 0.33$ while turbulent flows at $\omega > 0.5$. The equation shows the importance of having large surface electrode area, high rates of mass transport k_m, and high concentration.

3 Design and Characterization of Electrochemical Reactors

The need for characterizing and modeling electrochemical reactors for EAOPs resides on the intensification of the wastewater treatment process taking into account the kinetic and mass transport conditions mentioned in the previous section. Modeling helps to achieve the optimal design of the electrochemical reactor, its understanding, and the design of compact technologies with rapid degradation rates, high mineralization current efficiencies (MCEs), and low electric energy consumptions (E_c). In order to achieve high MCEs, the desirable electrochemical reactions need to be controlled, avoiding as much as possible any parasitic side reactions. In this context, the experimental characterization and theoretical modeling of electrochemical reactors plays a crucial role, because it helps to design the correct shape and size of the reactor components, such as type and length of electrodes, nature and form of the turbulent promoters, electrolyte distributors, frames, and current feeders. In addition, the combination of the experimental characterization and modeling of transport phenomena, such as hydrodynamics, mass transport, heat transfer, and potential and current distributions, allows determining the optimal operational conditions to be applied to the electrochemical reactor.

3.1 Experimental Characterization

3.1.1 Pressure Drop and Non-ideal Flow Dispersion

In electrochemical reactors, the experimental characterization of flow pattern is widely explored by researchers because it offers mathematical simplicity, compared with those CFD predictions, and their contribution from the design of

electrochemical cells, flow, and pressure expressions is well described by empirical correlations and simple mathematical functions. The residence time distribution and pressure drop measurements are the typical techniques to characterize experimentally fluid flow patterns and pressure drops within electrochemical flow cells.

Pressure drop measurements are employed to determine the pumping energy requirements necessary to allow passage of the electrolyte streams within the electrochemical cell. The empirical pressure drop (ΔP) is typically described by a logarithmic function of the dimensionless Reynolds number:

$$\Delta P = a\mathrm{Re}^{b} \tag{10}$$

where the Reynolds relates to the inertial and viscous forces of the electrolyte flow and is described as:

$$\mathrm{Re} = \frac{ud}{\upsilon} \tag{11}$$

The coefficient a and exponent b are typically associated with geometric factors and flow patterns (i.e., laminar and turbulent flow in empty channels), respectively. The variables u, d, and υ are the mean linear flow rate, characteristic length of the electrochemical reactor, and kinematic viscosity. The characteristic length in rectangular flow cells is equal to the hydraulic diameter, while in rotating cylinder cells, d is defined as the diameter of the inner rotating cylinder. In packed bed electrochemical reactors, filled with particulate material as electrodes, the diameter of the spheroid type material employed takes the role of the characteristic length.

Several authors also report the mass transport coefficients as a function of the pressure drop (Eq. 12), which is realized considering that the mass transport parameter depends on the electrode geometry and the flow pattern (Eq. 13).

$$k_m A = a\Delta P^{b} \tag{12}$$

$$k_m A = a\mathrm{Re}^{b} \tag{13}$$

Table 1 shows the experimental correlations of pressure drop over the well-known FM01-LC reactor extensively employed in EAOPs. In the case of the single-cell configuration, the a and b parameters increase in the filled channel (with turbulence promoter) with respect to the empty channel. This is attributed to the obstruction of the transversal area by the plastic net (turbulence promoter), where the electrolyte flows, which demands higher energy from the pumps. Meanwhile, the pressure drop increases in the stack of three empty undivided cells, indicating that this configuration demands higher energy pump consumption. The mass transport for 3D electrodes indicates that the metal foam electrodes present a higher $k_{\mathrm{m}}A$ for a similar pressure drop across the expanded metal electrodes. The presence of porous electrodes demands higher pumps power, although mass transport is enhanced.

Table 1 Experimental values of pressure drop over the FM01-LC reactor

Configuration	$a \times 10^2$	b	Correlation	Ref.
Empty single cell	0.69	1.39	$\Delta P = a\mathrm{Re}^b$	[26]
Filled single cell with PTFE turbulence promoter	1.69	1.54	$\Delta P = a\mathrm{Re}^b$	[26]
Stack of three empty undivided cells	0.028	2.88	$\Delta P = a\mathrm{Re}^b$	[27]
Expanded metal configuration (single cell)	0.29	0.44	$k_\mathrm{m}A = a\Delta P^b$	[28]
Metal foam (single cell)	0.38	0.47	$k_\mathrm{m}A = a\Delta P^b$	[28]

On the other hand, in filter press type reactors the ideal plug flow model is expected, although this cannot be guaranteed since the electrolyte kinetic energy losses, attributed to the friction of the liquid on the walls, induce plug flow deviations. Several models have been developed to describe these plug flow variations, which are typically obtained by means of experiments of the residence time distribution (RTD). The most common model used to describe plug flow deviations is the dispersion plug flow (DPF) model:

$$\frac{\partial C}{\partial \theta} = \frac{1}{\mathrm{Pe}} \frac{\partial^2 C}{\partial x^2} - \frac{\partial C}{\partial x} \tag{14}$$

where C is the dimensionless tracer concentration ($=c/c_0$), θ is the dimensionless time ($=t/\tau$), Pe is the dimensionless Peclet number ($=uL_x/D_{ax}\xi$), and x is the dimensionless axial length ($=X/L_X$). Here, c is the tracer concentration at any time, c_0 is the initial tracer concentration, X is the axis coordinate along the FM01-LC reactor length, L_x is the axial length, u is average mean linear liquid velocity in an empty channel, ξ is the bed void fraction (in empty channels, $\xi = 1$), and D_{ax} is the dispersion coefficient.

RTD experiments allow obtaining D_{ax}, which accounts for the plug flow deviations. Figure 2 shows the experimental and adjusted RTD curves in an empty flow channel of a filter press electrolyzer. Close agreement between simulation and experimental data was attained. The dispersion coefficient tends to increase with flow velocity.

The RTD impacts directly to the conversion because the fluid elements have different residence times. These fluctuations create variations of the concentration at the exit of the cell. In the ideal plug flow model, where there is no dispersion degree of the electrolyte, the concentration of the electroactive species leaves the reactor at $\theta = 1$.

Other models of RTD applied to filter-press flow reactors have been extensively investigated [29]. CFD techniques have been extensively performed to model and simulate the RTD showing excellent agreement between experiments and simulations; the latter will be discussed below.

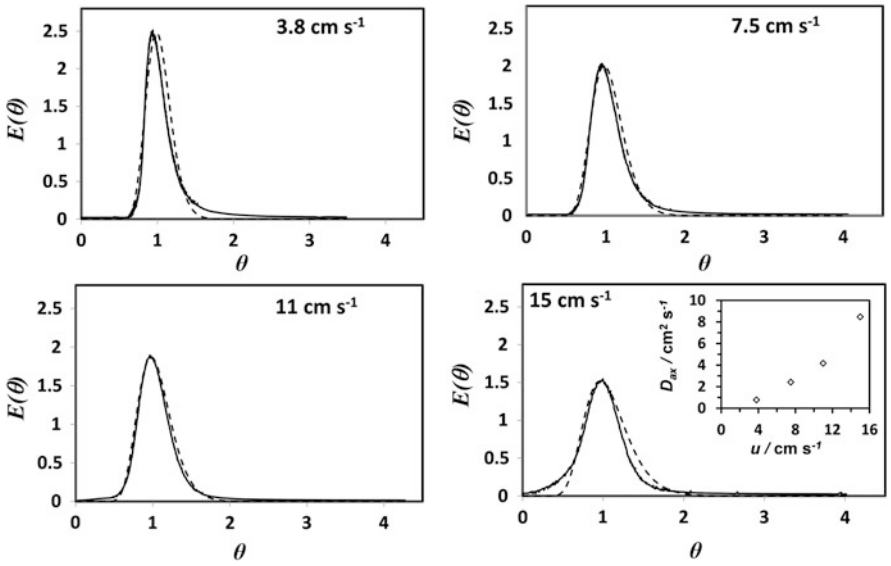

Fig. 2 Comparisons of experimental (—) and theoretical (----) RTD curves in the empty channel of the FM01-LC reactor at different flow velocities. The simulation was performed by the DPF model. Inset shows the axial dispersion coefficient versus flow velocity

3.1.2 Mass Transport Characterization

The experimental mass transport characterization is an important tool for evaluating the performance of an electrochemical reactor under mass transport control. The global mass transport coefficient is directly related to the global limiting current, as derived from (Eq. 2), and the electrolyte flow rate. The mass transport coefficient can be expressed in two types of correlations, the former, in terms of mean linear flow rates according to Eq. (15), and the second, by means of the dimensionless numbers, through Eq. (16).

$$k_{\mathrm{m}} = au^{b} \tag{15}$$

$$\mathrm{Sh} = a\mathrm{Re}^{b}\mathrm{Sc}^{0.33} \tag{16}$$

where a and b are empirical constants. The Sherwood number ($\mathrm{Sh} = k_{\mathrm{m}}u/D$) relates the convective mass transport to molecular diffusion, and the Schmidt number ($\mathrm{Sc} = \upsilon/D$) correlates momentum diffusivity and molecular diffusion; the variable D is the diffusion coefficient. It is worth mentioning that the mass transport coefficient depends on the geometry of electrochemical reactor, electrolyte properties, and electrochemical systems [29]. Table 2 summarizes the mass transport correlations of different electrochemical reactors.

From the analysis of Table 2, we can observe that the a and b parameters vary depending on the type of reactor. In the case of the FM01-LC reactor, the mass

Table 2 Mass transport correlations ($Sh = aRe^bSc^c$) for the reduction of ferricyanide, for type of reactors

Channel configuration	Re and Re_p range	*a*	*b*	Cathode material	Ref.
Filter-press type reactors					
FM01-LC					
Empty channel	$200 < Re < 1{,}000$	0.22	0.71	Stainless steel	[32]
Channel with turbulence promoter	$200 < Re < 1{,}000$	0.74	0.62	Stainless steel	[32]
3-D electrode: reticulated metal	$264 < Re_p < 1{,}065$	3.81	0.68	Nickel foam	[33]
DIACELL™					
Empty channel	$25 < Re < 100$	0.69	0.36	BDD	[34]
Empty channel	$100 < Re < 2{,}500$	0.14	0.45	BDD	[34]
ElectroSyn™					
3-D electrode: reticulated metal	$300 < Re < 2{,}300$	0.32	0.61	Nickel foam	[35]
Stirred type reactor					
Rotating cylinder					
Inner rotating cylinder	$112 < Re < 1.62 \times 10^5$	0.079	0.7	Nickel	[36]

The parameter *c* is equal to 0.33 and 0.356 for filter-press type and rotating cylinder reactor
Re_p is the particle Reynolds number

transport enhances in the following order: empty channel < channel with turbulence promoter < channel with reticulated electrode. In the empty rectangular channel, the laminar flow is developed between $100 < Re < 2{,}300$, while the turbulent flow is achieved at $Re > 2{,}300$. In smooth rotating cylinder electrodes, the turbulent flow is achieved at $Re > 100$. In this latter type of reactor, the turbulent mass transport predominates.

Recently, the characterization of mass transport during the reduction of dissolved oxygen to yield hydrogen peroxide was reported using graphite felt (GF), reticulated vitreous carbon (RVC), and planar BDD as cathodes [30]. The empirical law of mass transport described by Eq. (15) revealed a chaotic flow pattern within the porous structures of GF and RVC, which favored the mass transport. Mass transport was especially enhanced in the cell with GF due to its larger volumetric area, resulting in greater limiting current values.

On the other hand, in many papers about the anodic oxidation (AO) on BDD electrodes several authors use the Eq. (2), for the ferri/ferrocyanide electrochemical system, to calculate the mass transport value k_m, and subsequently the limiting current is evaluated and applied to the BDD–electrolyte interface by means of the following equation [31]:

$$I_L = 4AFk_mCOD \tag{17}$$

This expression considers that all the organic compounds, present in the electrolyte, can be completely oxidized to CO_2. Here, $n = 4$ and COD is the chemical oxygen demand. This methodology has been extended to PbO_2 electrodes.

The experimental evaluation of electrochemical reactors used in EAOPs requires the analysis of RTD to avoid undesirable flow patterns that impact on the performance of the electrochemical cell. Following this analysis, the experimental mass transport characterization is essential to find the operational conditions that include the electrolyte flow rate and the limiting current density being applied to the electrochemical reactor. The empirical mass transport correlations are helpful for scaling-up purposes.

3.2 Theoretical Characterization (Modeling and Simulation)

The modeling of hydrodynamics, mass transport, and current distribution in electrochemical reactors can be performed by CFD techniques, which allow measuring local variables and parameters such as velocity, concentration, mass transport coefficients, potential, and current. The CFD simulations with commercial and open access software which employ mesh methods in 2D and 3D are common practice. In the first instances, the electrochemical reactor is used to establish the domain of the numerical simulation. The numerical methods typically employed are the finite element and volume element methods, among others. The numerical methods provide a similar result if a sensitivity analysis of the mesh is performed. Taking the latter into account, a systematic study of the calculations of hydrodynamics, mass transport, and current and potential distribution, emphasizing their useful to guarantee acceptable mineralization current efficiencies and energy consumptions, is presented below.

3.2.1 Simulation of Hydrodynamics in a Filter-Press Type Electrolyzer

Figure 3a, b shows the simulation domain in the empty and filled channels used for the computational analysis. The cell dimensions are shown elsewhere [29].

The mean linear flow rates studied were comprised in the range between (0.038 and 0.15 m s^{-1}) giving Reynolds number between 300 and 1,500, characteristic of a laminar flow for the empty channel. Thus, the solution of the Navier–Stokes (NS) and diffusion-convection equations were used for the velocity field and RTD determinations. On the other hand, the same flow rates for the channel in the presence of the net plastic were used. However, since the net plastic creates high velocity streams causing 3D flow instabilities and eddy formations, we solve the Reynolds averaged Navier–Stokes (RANS) and the averaged diffusion-convection equations for the simulations.

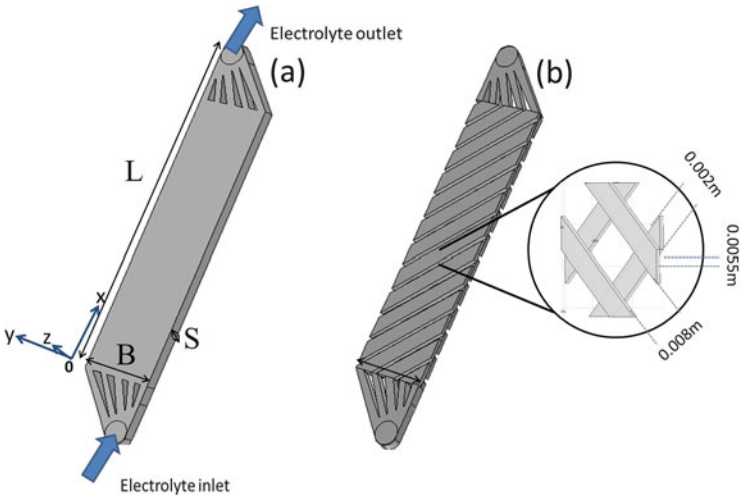

Fig. 3 Simulation domain established to implement the CFD simulation: (**a**) empty channel and (**b**) turbulence promoter-filled channel. The inset enlarges the turbulence promoter. Adapted from [37]

Laminar Flow (Empty Channel)

Under laminar flow conditions, the equations of the model for an incompressible fluid flow can be stated as follows. The Navier–Stokes and the continuity equations in steady state are:

$$\rho(\boldsymbol{u}\cdot\nabla)\boldsymbol{u} = \nabla\cdot[-P+\mu(\nabla\cdot\boldsymbol{u})] \tag{18}$$

$$\nabla\cdot(\rho\boldsymbol{u}) = 0 \tag{19}$$

where μ denotes the dynamic viscosity of the fluid, $\boldsymbol{u}$ is the velocity vector, P is the pressure, and ρ is the density of the fluid. To solve Eqs. (18) and (19), the corresponding boundary conditions are considered as follows:

1. At the inlet, a normal inflow velocity was used, $\boldsymbol{u} = -\boldsymbol{n}U_0$, where $\boldsymbol{n}$ is the unit normal vector,
2. A value of pressure at the outlet, $\rho(\boldsymbol{u}\cdot\nabla)\boldsymbol{u} = \nabla\cdot[-P+\mu(\nabla\cdot\boldsymbol{u})] = -\boldsymbol{n}P_0$,
3. In the walls, no slip consideration was set: $\boldsymbol{u} = 0$,

where U_0 is the inflow velocity and P_0 is the pressure at the exit of the cell.

Turbulent Flow (Filled Channel)

The net plastic used as a turbulence promoter usually performs a chaotic hydrodynamic flow pattern. Then, the fluid flow must be stated with a turbulence model. In this case, the RANS equations are applied:

$$\rho(\boldsymbol{u}\cdot\nabla)\boldsymbol{u} = -\nabla P + \nabla\cdot\left((\mu+\mu_{\mathrm{T}})\left(\nabla\cdot\boldsymbol{u} + (\nabla\cdot\boldsymbol{u})^{\mathrm{T}}\right)\right) \tag{20}$$

where the so-called Reynolds stresses can be expressed in terms of a turbulent viscosity μ_{T}, according to the standard k–ε turbulence model:

$$\mu_{\mathrm{T}} = \rho C_{\mu}\frac{k^2}{\varepsilon} \tag{21}$$

where k is the turbulent kinetic energy, and ε is the turbulent energy dissipation rate. A detailed description of the typical boundary conditions to solve Eqs. (20) and (21) can be consulted elsewhere [38].

Results and Discussion

Figure 4a, b shows the velocity field profile plots for an inflow velocity of 0.11 m s^{-1} in the empty and filled channels. The effect of inlet flow distributor on the velocity can be observed in the empty channel, which develops a jet flow. This flow deviation is avoided by the net-like spacer (classical turbulence promoter type D) because it homogenizes the velocity field inside the channel. This last effect is a desirable condition to guarantee an acceptable fluid flow dispersion, mass transport enhancement, and uniform current distribution during the scaling-up.

Comparisons of the experimental and simulated RTD in the empty and filled channel as a function of the dimensionless residence time (not shown) demonstrated excellent agreement between the theoretical and experimental RTD curves. Recently, the RTD in a multi-electrode stack has been modeled. The results demonstrate the powerful potential of CFD simulation to predict non-ideal flow deviations in very complex geometries [27].

The use of CFD techniques leads to visualize the fluid pattern within the electrode gap in electrochemical reactors. CFD visualizations are a powerful tool to prevent undesirable flow deviations such as stagnant zones, back mixing, and recirculation of electrolyte. These numerical models can be extended to design novel 3D electrodes, such as BDD or DSA® foams, expanded metal electrodes, and granular packed bed structures, among others. In addition, the CFD tools are useful in the design of net-like spacers used as turbulence promoters and during the scale-up of electrochemical reactors.

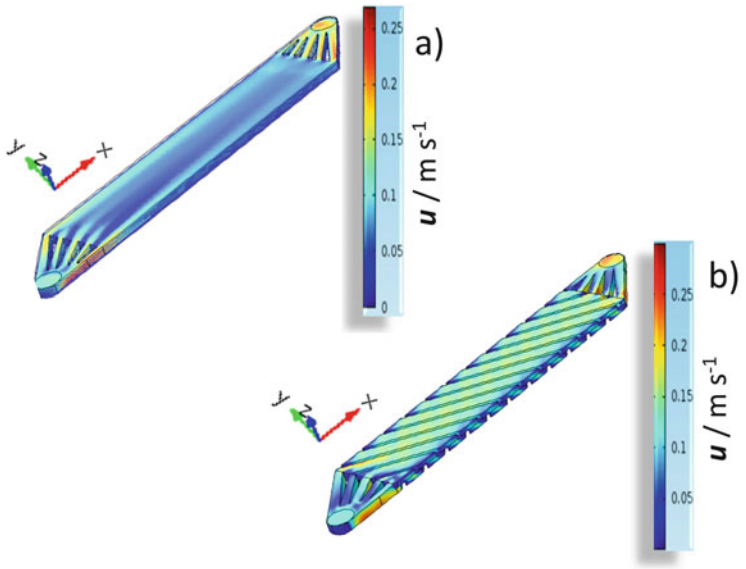

Fig. 4 Simulated velocity field magnitude at characteristic inflow velocity of 0.11 m s^{-1}. (**a**) Empty channel, (**b**) turbulence promoter-filled channel. Adapted from [37]

3.2.2 Simulations of the Secondary Current Distribution Along the BDD Plate During the Formation of Hydroxyl Radicals from the Water Discharge

In electrolytic cells containing large extended electrode area, the control of the potential and current is mandatory to guarantee the selectivity of the desired electrochemical reactions and to avoid undesirable side reactions. Here, we present the primary and secondary current distribution along a BDD plate fitted into the FM01-LC reactor. Oxidation of water to yield BDD($^{\bullet}$OH) in acidic sulfate electrolyte was used as an example of an electrochemical system.

Formulation of the Numerical Simulation

The domain was considered inside the cell as a parallelepiped shape similar to that shown in Fig. 3a, and it was assumed that the potential drop along the conductive BDD material was negligible. In dilute solutions, the current density, j, at any point inside the parallelepiped cell is determined by the gradient of the local potential, ϕ, by means of the Ohm's Law of the ionic conductance:

$$j = -\kappa \nabla \phi \tag{22}$$

Table 3 Boundary conditions to solve the Laplace Eq. (23)

	Primary current distribution	Secondary current distribution
At BDD anode	$\phi = \phi_a$	$-\kappa \frac{\partial \phi}{\partial \xi} = j_0 \exp\left(\frac{\eta}{b_a}\right)$
At platinized cathode	$\phi = \phi_c$	$-\kappa \frac{\partial \phi}{\partial \xi} = j_{ave}$
At isolants	$-\kappa \frac{\partial \phi}{\partial \xi} = 0$	$-\kappa \frac{\partial \phi}{\partial \xi} = 0$

where κ is the ionic conductivity of the electrolyte. While the potential distribution in the electrolyte is described by the Laplace equation:

$$\nabla^2 \phi = 0 \tag{23}$$

Equation (23) is resolved first with corresponding boundary conditions, which are shown in Table 3, for the primary and secondary problem. Then, the current distribution is determined using Eq. (22).

In Table 3, ϕ_a, ϕ_c are surface potentials adjacent to anode and cathode; in practice, these are equal to the open circuit potentials, ξ is the normal component to the surface, j_0 is the exchange current density, η is the potential difference between the applied potential, and ϕ_a ($=V - \phi_a$), b_a is the anodic Tafel slope, and j_{ave} is the averaged current density at the cathode.

The numerical solution of transport equations was solved by the finite element software (COMSOL Multyphisics®). More details of the methodology used in the numerical simulations can be consulted in [39].

Results and Discussion

Figure 5 shows the normalized primary current distribution on the BDD surface (at $z = 0$) versus the normalized BDD length, x/L, at heights (y) of 0, 0.25, 0.8, and 2 cm. Border edges are located close to $x/L = 0$ and $x/L = 1$, being more important near the curved corners. However, these edge effects differ with a magnitude order of 1×10^{-5}; therefore, the primary current distribution at BDD anode in the FM01-LC reactor can be considered uniform. This figure also shows the secondary current distribution evaluated at an overpotential, $\eta = 1.7$ V, where the hydroxyl radical formation occurs. A clear homogeneous current distribution, as predicted, was observed. The disappearance of the border effects in the secondary current distribution is related to the charge transfer resistance of water discharge on the BDD surface.

The homogeneous primary and secondary current distributions in the FM01-LC were developed considering the absence of isolated walls in the plane $x - y$, where the BDD is fitted, and by the 90° angle, forming by the polypropylene frame and the electrodes. The latter confirms the appropriateness of the engineered cell design and is consistent with several studies performed by our group where current efficiencies

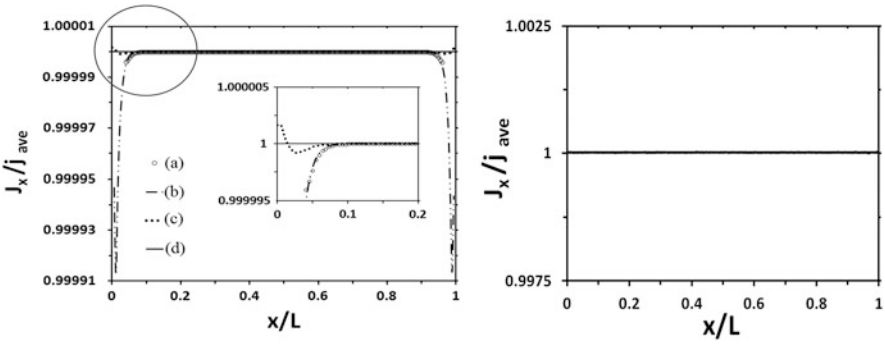

Fig. 5 Normalized primary (*left*) and secondary (*right*) current distribution profiles along the BDD working electrode at different heights: (a) $y = 0$ cm, (b) $y = 0.25$ cm, (c) $y = 0.8$ cm, and (d) $y = 2$ cm. Secondary simulations were performed at $\eta = 1.7$ V. Adapted from Ref. [39], Copyright 2013, with permission from Elsevier

during electrochemical incineration of cresols, indigo dye, and diclofenac using BDD as anode achieved current efficiencies greater than 80% [40–42].

The simulation of the tertiary current distribution along the BDD electrode during the anodic oxidation of organic compounds might be described by means of the limiting current density Eq. (17). The local mass transport coefficient, k_m, can be numerically evaluated via the empirical correlation described by Eq. (15), where the local velocity magnitude in this equation should come from the solution of NS or RANS equations. The simulation of the tertiary current distribution during anodic oxidation of organics has not yet been reported; however, for the purpose of visualizing the pattern of this tertiary distribution, readers can consult a paper published by our groups [38].

3.2.3 The Modeling of a Solar Photoelectro-Fenton Flow Plant

Figure 6 presents a schematic diagram of a pre-pilot solar photoelectron-Fenton (SPEF) flow plant in recirculation mode of operation that has been used for modeling. This plant couples a filter-press flow cell (the FM01-LC) in series with a compound parabolic collector (CPC) photoreactor. The mineralization of 10 dm^3 of the antibiotic erythromycin (ERY) was used as a model to test the system.

Mathematical Model

A parametric model including the mass balance in the electrochemical reactor and the CPC reservoir tank in one dimension was implemented. The model considers that the potential distribution on the GF is small, which avoids the side hydrogen evolution Reaction (HER).

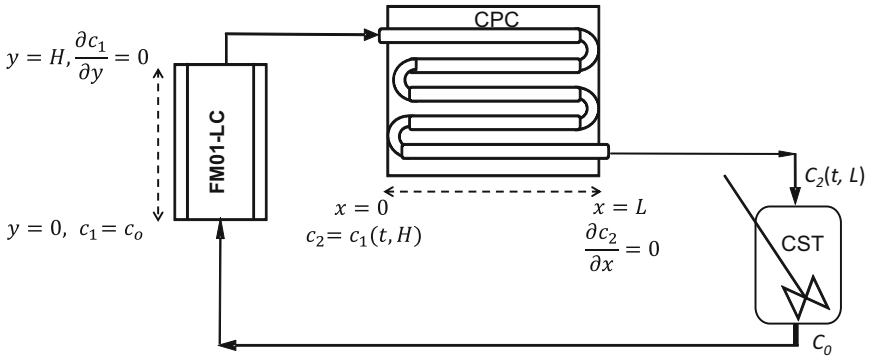

Fig. 6 Setup of the SPEF flow plant in pre-pilot scale. Reprinted from Ref. [43], Copyright 2017, with permission from Elsevier

The dissolved organic carbon (DOC) decay from ERY solutions treated here involves several Reaction steps and kinetic constants such as the electrogeneration of H_2O_2, the Fenton's Reaction, photocatalytic reactions, and hydroxylation/dehydrogenation of the compounds leading to the formation of complex organic by-products and radicals during the degradation [44–46]. In order to construct a working model that follows the gradual depletion of DOC over time in recirculation mode, the following strategy was utilized: (1) the dispersion model expression for the FM01-LC, (2) the dispersion model with a global Reaction rate term for the CPC, and (3) the mass balance equation in the continuous stirred tank (CST) in transient regime. The abovementioned conservation equations were solved via finite element method using the boundary conditions shown in Fig. 6. In this parametric model, the Reaction order that better fitted the experimental DOC–time curves was zero, as determined after several simulation trials. A detailed description of the considerations of this model can be consulted in Ref. [43].

Results and Discussion

Figure 7 depicts the simulated DOC–time plots, as solid lines determined from the proposed parametric model, and as symbols from experimental data, obtained for 50, 100, 150 mg dm^{-3} ERY solution with 0.50×10^{-3} mol dm^{-3} Fe^{2+} at pH 3.0 and $j = 0.16$ mA cm^{-2} at $Q = 3.0$ dm^3 min^{-1}. Close agreement between theoretical and experimental data was obtained. The model predicts well the experiments if the oxygen reduction to yield H_2O_2 is favored, avoiding HER; in other words, the applied current density to favor the oxygen reduction Reaction (ORR) should give a cathodic potential between $-0.4 < E < 0.1$ V versus SHE, because at $E < -0.4$ V versus SHE, the parasitic HER occurs [30] and inhibits the SPEF process. Additional simulations including, i.e., the influence of current density, Fe (II) concentration, and electrode potential on ERY degradation, can be found in [43].

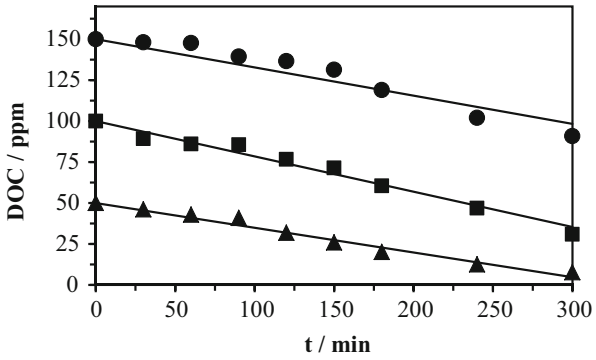

Fig. 7 DOC removal with electrolysis time for the SPEF experiments with initial DOC of (*filled triangles*) 50 mg dm^{-3}, (*filled squares*) 100 mg dm^{-3}, and (*filled circles*) 150 mg dm^{-3}, at $Q = 3.0\ dm^3\ min^{-1}$. *Solid lines* (—) are the theoretical data determined from the parametric model taking C_0 = DOC. Electrolyte: 0.050 mol dm^{-3} Na_2SO_4 with 0.50×10^{-3} mol dm^{-3} Fe^{2+} at pH = 3.0. The cathodic current density was 0.16 mA cm^{-2}. Reprinted from Ref. [43], Copyright 2017, with permission from Elsevier

It is important to remark that the parametric model developed here was designed to understand and correlate the experimental DOC decay with time. In other words, this model allowed determining the global apparent Reaction term, without the contribution of the non-ideal flow deviations in the FM01-LC and CPC reactors. In this global apparent Reaction term, $^{\bullet}OH$ is presupposed as the most powerful oxidant, although slower Reactions with other weaker oxidizing species like H_2O_2 and $HO_2^{\bullet}$ are feasible.

Modeling strategy is a basic tool for scaling-up of EAOPs, since if the theoretical approach (in pre-pilot scale) reproduces the experimental data the electrochemical engineer can extend the model to design a pilot plant. A very important factor to mention is the fact the scale-up process should satisfy the similarities of geometry, momentum, chemical reaction and mass transport, electric field, and heat transfer; the latter analysis was out of the scope of this chapter, but interested readers should consult Ref. [47].

4 Further Developments and Perspectives

In order to design electrochemical reactors for EAOPs, CFD simulations with the experimental characterization help to (1) develop novel electrochemical cells involved in EAOPs and (2) characterize the Reaction environment of existing reactors. These models can be extended to design novel 3D electrodes, such as BDD or DSA® foams, expanded metal electrodes, and granular packed bed structures; in addition, CFD techniques can be used to design novel net-like spacers used as turbulence promoters that favor mass transport. The characterization of the

Reaction environment such as hydrodynamics, mass transport, heat transfer, and potential and current distributions, allows determining the optimal operational conditions to be applied to the reactors.

The optimal design of the electrochemical reactors allows developing compact volumes with rapid degradation rates, high mineralization current efficiencies, and low electric energy consumptions. One of the most valuable parameters, not often considered in the design and evaluation of advanced oxidation processes, is the space–time yield.

The challenges reside on the modeling of biphasic systems (including gas H_2/O_2 release), which have not been yet characterized, even when it is well known that gas bubbling increases the electrolytic energy consumption. The modeling of flow plants (containing several reactors and unit operations) also deserves special attention. The mathematical modeling is crucial during the scale-up of EAOPs.

References

1. Wendt H, Kreysa G (2010) Electrochemical engineering; science and technology in chemical and other industries. Springer, Berlin
2. Pletcher D, Walsh FC (1990) Industrial electrochemistry, 2nd edn. Chapman and Hall, London
3. Bebelis S, Bouzek K, Cornell A, Kelsall GH, Ferreira MGS, Lapicque F, Ponce de León C, Rodrigo MA, Walsh FC (2013) Highlights during the development of electrochemical engineering. Chem Eng Res Des 91:1998–2020
4. Quan X, Cheng Z, Chen B, Zhu X (2013) Electrochemical oxidation of recalcitrant organic compounds in biologically treated municipal solid waste leachate in a flow reactor. J Environ Sci 25:2023–2030
5. Brillas E, Garrido JA, Rodríguez RM, Arias C, Cabot PL, Centellas F (2008) Wastewaters by electrochemical advanced oxidation processes using a BDD anode and electrogenerated H_2O_2 with Fe(II) and UVA light as catalysts. Port Electrochim Acta 26:15–46
6. Vasconcelos VM, Ponce-de-León C, Nava JL, Lanza MRV (2016) Electrochemical degradation of RB-5 dye by anodic oxidation, electro-Fenton and by combining anodic oxidation-electro-Fenton in a filter-press flow cell. J Electroanal Chem 765:179–187
7. Bedolla-Guzman A, Feria-Reyes R, Gutierrez-Granados S, Peralta-Hernández JM (2017) Decolorization and degradation of reactive yellow HF aqueous solutions by electrochemical advanced oxidation processes. Environ Sci Pollut Res 24:12506–12514
8. Ting WP, Lu MC, Huang YH (2008) The reactor design and comparison of Fenton, electro-Fenton and photoelectro-Fenton processes for mineralization of benzene sulfonic acid (BSA). J Hazard Mater 156:421–427
9. Koparal AS, Yavuz Y, Gürel C, Öğütveren UB (2007) Electrochemical degradation and toxicity reduction of C.I. Basic Red 29 solution and textile wastewater by using diamond anode. J Hazard Mater 145:100–108
10. Yavuz Y, Shahbazi R (2012) Anodic oxidation of reactive black 5 dye using boron doped diamond anodes in a bipolar trickle tower reactor. Separ Purif Tech 85:130–136
11. Anotai J, Su CC, Tsai YC, Lu MC (2010) Effect of hydrogen peroxide on aniline oxidation by electro-Fenton and fluidized-bed Fenton processes. J Hazard Mater 183:888–893
12. Hussain SN, Roberts EPL, Asghar HMA, Campen AK, Brown NW (2013) Oxidation of phenol and the adsorption of breakdown products using a graphite adsorbent with electrochemical regeneration. Electrochim Acta 92:20–30

13. Cusick RD, Ullery ML, Dempsey BA, Logan BE (2014) Electrochemical struvite precipitation from digestate with a fluidized bed cathode microbial electrolysis cell. Water Res 54:297–306
14. Valenzuela AL, Vázquez-Medrano R, Ibáñez JB, Frontana-Uribe BA, Prato-Garcia D (2017) Remediation of diquat-contaminated water by electrochemical advanced oxidation processes using boron-doped diamond (BDD) anodes. Water Air Soil Pollut 228:67
15. Bergmann MEH, Rollin J, Iourtchouk T (2009) The occurrence of perchlorate during drinking water electrolysis using BDD anodes. Electrochim Acta 54:2102–2107
16. Recio FJ, Herrasti P, Vazquez L, Ponce de León C, Walsh FC (2013) Mass transfer to a nanostructured nickel electrodeposit of high surface area in a rectangular flow channel. Electrochim Acta 90:507–513
17. Nava-M de Oca JL, Sosa E, Ponce de León C, Oropeza MT (2001) Effectiveness factors in an electrochemical reactor with rotating cylinder electrode for the acid-cupric/copper cathode interface process. Chem Eng Sci 56:2695–2702
18. Fleischmann M, Ibrisagić Z (1980) Electrical measurement in bipolar trickle reactors. J Appl Electrochem 10:151–156
19. Comninellis C (1994) Electrocatalysis in the electrochemical conversion/combustion of organic pollutants for waste water treatment. Electrochim Acta 39:1857–1862
20. Pletcher D, Walsh FC (1992) Three-dimensional electrodes. In: Genders JD, Weinberg NL (eds) Electrochemical technology for a cleaner environment. The Electrosynthesis Company Inc, Lancaster, NY
21. Harrington T, Pletcher D (1999) The removal of low levels of organics from aqueous solutions using Fe(II) and hydrogen peroxide formed in situ at gas diffusion electrodes. J Electrochem Soc 146:2983–2989
22. Recio FJ, Herrasti P, Sirés I, Kulak AN, Bavykin DV, Ponce de León C, Walsh FC (2011) The preparation of PbO_2 coatings on reticulated vitreous carbon for the electro-oxidation of organic pollutants. Electrochim Acta 56:5158–5165
23. He Y, Lin H, Wang X, Huang W, Chen R, Li H (2016) A hydrophobic three-dimensionally networked boron-doped diamond electrode towards electrochemical oxidation. Chem Commun 52:8026–8029
24. Bard AJ, Faulkner LR (2001) Electrochemical methods; fundamentals and applications, 2nd edn. Wiley, Hoboken, NJ
25. Walsh FC (1993) A first course in electrochemical engineering. The Electrochemical Consultancy, Romsey
26. Trinidad P, Walsh FC (1996) Hydrodynamic behaviour of the FM01-LC reactor. Electrochim Acta 41:493–502
27. Sandoval MA, Fuentes R, Walsh FC, Nava JL, Ponce de León C (2016) Computational fluid dynamics simulations of single-phase flow having a stack of three cells. Electrochim Acta 216:490–498
28. Bengoa C, Montillet A, Legentilhomme P, Legrand J (2000) Characterization and modeling of the hydrodynamic behaviour in the filter-press-type FM01-LC electrochemical cell by direct flow visualization and residence time distribution. Ind Eng Chem Res 29:2199–2206
29. Rivera FF, Ponce de León C, Walsh FC, Nava JL (2015) The reaction environment in a filter-press laboratory reactor: the FM01-LC cell. Electrochim Acta 161:436–452
30. Coria G, Pérez T, Sirés I, Nava JL (2015) Mass transport studies during dissolved oxygen reduction to hydrogen peroxide in a filter-press electrolyzer using graphite felt, reticulated vitreous carbon and boron-doped diamond as cathodes. J Electroanal Chem 257:225–229
31. Gherardini L, Michaud PA, Panizza M, Comninellis C, Vatistas N (2001) Electrochemical oxidation of 4-chlorophenol for wastewater treatment. J Electrochem Soc 148:D78–D82
32. Brown CJ, Pletcher D, Walsh FC, Hammond JK, Robinson D (1992) Local mass transport effects in the FM01 laboratory electrolyser. J Appl Electrochem 22:613–619
33. Griffiths M, Ponce de León C, Walsh FC (2005) Mass transport in the rectangular channel of a filter-press electrolyzer (the FM01-LC reactor). Am Int Chem Eng J 51:682–687

34. Santos JLC, Geraldes V, Velizarov S, Crespo JG (2010) Characterization of fluid dynamics and mass-transfer in an electrochemical oxidation cell by experimental and CFD studies. Chem Eng J 157:379–392
35. Montillet A, Comiti J, Legrand J (1994) Application of metallic foams in electrochemical reactors of filter-press type. Part II: mass transfer performance. J Appl Electrochem 24:384–389
36. Eisenberg M, Tobias CW, Wilke CR (1954) Ionic mass transfer and concentration polarization at rotating electrode. J Electrochem Soc 101:306–320
37. Castañeda LF (2016) Evaluation of the performance of the FM01-LC reactor in the regeneration of H_2SO_4 from depleted baths by the electrodialysis process: theoretical and practical study. Dissertation, Centro de Investigación y Desarrollo Tecnológico en Electroquímica S.C.
38. Pérez T, Ponce de León C, Walsh FC, Nava JL (2015) Simulation of current distribution along a planar electrode under turbulent flow conditions in a laboratory filter-press flow cell. Electrochim Acta 154:352–360
39. Pérez T, León MI, Nava JL (2013) Numerical simulation of current distribution along the boron-doped diamond anode of a filter-press-type FM01-LC reactor during the oxidation of water. J Electroanal Chem 707:1–6
40. Butrón E, Juárez ME, Solis M, Teutli M, González I, Nava JL (2007) Electrochemical incineration of indigo textile dye in filter-press-type FM01-LC electrochemical cell using BDD electrodes. Electrochim Acta 52:6888–6894
41. Coria G, Nava JL, Carreño G (2014) Electrooxidation of diclofenac in synthetic pharmaceutical wastewater using an electrochemical reactor equipped with a boron doped diamond electrode. J Mex Chem Soc 58:303–308
42. Nava JL, Núñez F, González I (2007) Electrochemical incineration of *o*-cresol and *p*-cresol in the filter-press-type FM01-LC electrochemical cell using BDD electrodes in sulphate media at pH 0. Electrochim Acta 52:3229–3235
43. Pérez T, Sirés I, Brillas E, Nava JL (2017) Solar fotoelectron-Fenton flow plant modelling for the degradation of the antibiotic erythromycin in sulphate medium. Electrochim Acta 228:45–56
44. Brillas E, Martínez-Huitle CA (2015) Decontamination of wastewaters containing synthetic organic dyes by electrochemical methods. An updated review. Appl Catal Environ 166–167:603–643
45. Martínez-Huitle CA, Rodrigo MA, Sirés I, Scialdone O (2015) Single and coupled electrochemical processes and reactors for the abatement of organic water pollutants: a critical review. Chem Rev 115:13362–13407
46. Sirés I, Brillas E, Oturan MA, Rodrigo MA, Panizza M (2014) Electrochemical advanced oxidation processes: today and tomorrow. A review. Environ Sci Pollut Res 21:8336–8367
47. Goodridge F, Scott K (1995) Electrochemical process engineering: a guide to the design of electrochemical plant. Plenum Press, New York